Earth and Planetary Science Letters 544 (2020) 116388

Contents lists available at ScienceDirect

Earth and Planetary Science Letters

www.elsevier.com/locate/epsl

Temperature changes across the Paleocene-Eocene Thermal Maximum – a new high-resolution TEX_{86} temperature record from the Eastern North Sea Basin

Ella W. Stokke [a,*], Morgan T. Jones [a], Jessica E. Tierney [b], Henrik H. Svensen [a], Jessica H. Whiteside [c]

[a] Centre for Earth Evolution and Dynamics (CEED), University of Oslo, PO Box 1028 Blindern, 0315, Oslo, Norway
[b] The University of Arizona, Department of Geosciences, 1040 E 4th St, Tucson, AZ 85721, USA
[c] School of Ocean and Earth Science, National Oceanography Centre Southampton, University of Southampton, Southampton SO14 3ZH, United Kingdom

ARTICLE INFO

Article history:
Received 23 September 2019
Received in revised form 27 May 2020
Accepted 2 June 2020
Available online 15 June 2020
Editor: L. Robinson

Keywords:
PETM
North Atlantic Igneous Province
palaeotemperatures
TEX_{86}

ABSTRACT

The Paleocene-Eocene Thermal Maximum (PETM; ~55.9 Ma) was a hyperthermal event associated with large carbon cycle perturbations, sustained global warming, and marine and terrestrial environmental changes. One possible trigger and/or source of the carbon release that initiated the PETM is the emplacement of the North Atlantic Igneous Province (NAIP). This study focuses on an expanded section of marine clays and diatomite on Fur Island in northern Denmark, where the entire PETM sequence has been identified by a negative ~4.5‰ $\delta^{13}C_{TOC}$ excursion. This remarkably well-preserved section also contains >180 interbedded ash layers sourced from the NAIP, making it an ideal site for investigating the correlations between large-scale volcanism and environmental changes. This study provides a new and complete high-resolution TEX_{86}-derived sea-surface temperature (SST) reconstruction over the entire PETM and the post-PETM section (up to about 54.6 Ma). The palaeothermometry record indicates an apparent short-lived cooling episode in the late Paleocene, followed by a pronounced temperature response to the PETM carbon cycle perturbations with a ~10 °C SST increase during the PETM onset (up to ~33 °C). Extreme SSTs fall shortly after the PETM onset, and continue to decrease during the PETM body and recovery, down to anomalously cool SSTs post-PETM (~11–23 °C). Both phases of potential cooling coincide with proxies of active NAIP volcanism, suggesting a causal connection, although several overprinting non-thermal factors complicate interpretations of the TEX_{86} values. Indices of effusive and explosive NAIP volcanism are largely absent from the Danish stratigraphy during the PETM body, though a re-emergence toward the end of the PETM suggest NAIP volcanism might have played a role in the PETM termination in the North Sea. This new SST record completes the previous fragmented view of climate changes at this globally important PETM site, and indicates large temperature variations in the North Sea during the earliest Eocene that are possibly linked to NAIP volcanism.

1. Introduction

The Paleocene-Eocene Thermal Maximum (PETM) was an extreme hyperthermal event that punctuated the already greenhouse climate of the early Cenozoic (Zachos et al., 2010). The onset of the PETM was between 56.0 and 55.9 Ma (Charles et al., 2011; Westerhold et al., 2018; Zeebe and Lourens, 2019). It was associated with a global negative carbon isotopic excursion (CIE) of 3–5‰, attributed to the voluminous input of isotopically light carbon to the ocean and atmosphere (e.g. Zachos et al., 2010). This led to global ocean acidification, increased halocline stratification, and deep-sea anoxia (Babila et al., 2018; Kender et al., 2012; Schoon et al., 2015). On land, temperature changes were accompanied by hydrological changes and mammalian biogeographic reorganisation (e.g. McInerney and Wing, 2011). There are several hyperthermal events in the Palaeogene, but the PETM is unique in terms of both the magnitude and duration of warming (Zachos et al., 2010). Several sources of ^{12}C-rich carbon sources have been proposed for the PETM, including methane hydrates (Dickens et al., 1995), a bolide impact activating terrestrial carbon reservoirs (Schaller et al., 2016), and volcanic and thermogenic degassing from the North

* Corresponding author.
E-mail address: e.w.stokke@geo.uio.no (E.W. Stokke).

https://doi.org/10.1016/j.epsl.2020.116388

Atlantic Igneous Province (NAIP; Storey et al., 2007a; Svensen et al., 2004).

Existing PETM reconstructions of bottom-water temperature (BWT) and sea surface temperature (SST) show large variations in temperature increase, depending on depth, latitude, seawater chemistry, and the choice of proxy and calibration (Dunkley Jones et al., 2013; Frieling et al., 2017; Hollis et al., 2019). The severe ocean acidification and substantial deep-sea sediment dissolution during the PETM (Babila et al., 2018) puts severe limitations on applying carbonate-based temperature proxies such as Mg/Ca ratios and $\delta^{18}O$ compositions (e.g. Dunkley Jones et al., 2013). In contrast, the organic SST proxy TEX_{86} is based on the relative distribution of glycerol dialkyl glycerol tetraethers (GDGT) membrane lipids of marine *Thaumarchaeota* (Schouten et al., 2002), and is therefore unaffected by carbonate dissolution. Unlike Mg/Ca and $\delta^{18}O$, TEX_{86} is also insensitive to salinity and pH, and does not need to be corrected for ocean chemistry changes (Frieling et al., 2017; Hollis et al., 2019). This makes TEX_{86} ideal for investigating PETM temperatures, and has been applied to a number of PETM sections worldwide (Frieling et al., 2017; Schoon et al., 2015; Sluijs et al., 2006, 2011; Zachos et al., 2006).

The NAIP consists of extrusive and intrusive rocks around the modern Northeast Atlantic margins (Fig. 2). It was emplaced between 63-52 Ma, with the most voluminous activity occurring between 56-54 Ma during the opening of the North Atlantic (Storey et al., 2007b). Both the volcanic activity and contact metamorphism of organic-rich sediments are potentially major sources of carbon and other volatiles around the time of the PETM (Storey et al., 2007a; Svensen et al., 2004). The close proximity of the North Sea Basin to the NAIP makes this an ideal area to study climatic and volcanic proxies in the same section. NAIP-sourced tephras are numerous and widespread across the North Sea and in Denmark (e.g. King, 2016). A recent study also documented elevated Hg/TOC ratios in five continental shelf settings around the North Atlantic, interpreted as an indicator of elevated NAIP volcanic activity (Jones et al., 2019). An exceptionally well preserved and complete PETM section crops out on the island of Fur in northwest Denmark. It includes an expanded section of marine clays and interbedded ash layers, providing a unique opportunity to investigate a direct link between NAIP volcanism and PETM climatic changes.

Despite the clear advantages of studying the North Sea area, only one previous study has applied TEX_{86} in this region, presenting records from two localities in Denmark (Fur Island and Store Bælt; Schoon et al., 2015; Figs. 1, 2). They documented a SST increase of 7–12 °C at the PETM onset, followed by an overall decrease back to pre-PETM values by the end of the CIE recovery. They also suggested a pre-PETM cooling in the Danish strata (Schoon et al., 2015), which is at odds with the pre-PETM warming identified in most PETM sites globally (Frieling et al., 2019). However, the existing record from Fur is sparse, with only 10 samples from the onset and recovery of the CIE. This preliminary study lacks high-resolution in key intervals and does not include data from the CIE body and post-PETM strata. Here, we present a new high-resolution record from Fur covering the entire PETM from the latest Paleocene, including post-PETM sediments that have not been analysed before (Fig. 2). Constraining palaeotemperatures across significant climatic perturbations such as the PETM is crucial for understanding climate sensitivity and environmental change in the past, present, and future. By combining a detailed record of $\delta^{13}C_{TOC}$ and TEX_{86} SST estimates in conjunction with volcanic proxies, we aim to evaluate the link between the palaeotemperature record and NAIP volcanism in the North Sea basin and expand the global temperature dataset during the PETM.

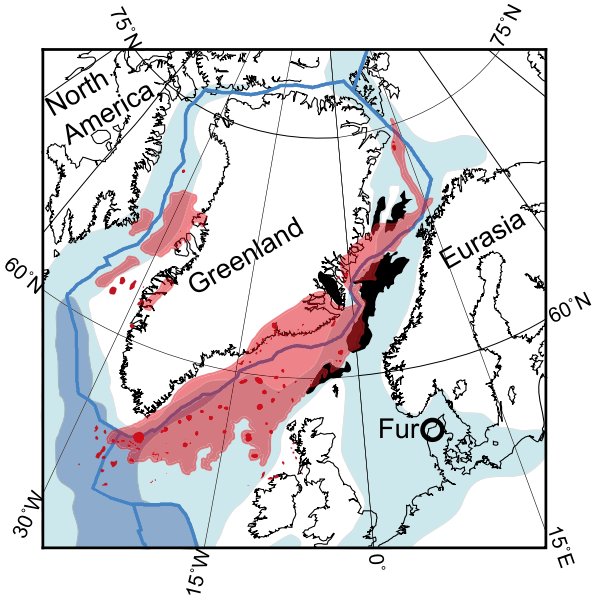

Fig. 1. Location of the island of Fur in a plate reconstruction at 56 Ma with the known extent of the NAIP indicated. Blue lines: plate boundaries. Black lines: present day coastlines. Light and dark blue areas: shelf and deep marine areas respectively. Light red areas: Known extent of subaerial and submarine volcanism from the NAIP. Dark red: individual volcanic centres. Black areas: extent of known NAIP sill intrusions in sedimentary basins. Figure modified from Jones et al. (2019). (For interpretation of the colours in the figure(s), the reader is referred to the web version of this article.)

2. Materials and methods

2.1. Stratigraphy and sampling

2.1.1. Stratigraphy

Fur is a small island (22 km^2) in Limfjorden, Denmark (Fig. 2). During the latest Paleocene and earliest Eocene, thermal uplift around the NAIP led to the almost complete isolation of the North Sea Basin (Knox et al., 2010). Water depths around the study area were outer neritic, probably between 100–200 m (Knox et al., 2010; Schoon et al., 2015). The Paleocene-Eocene transition is marked at Fur by a shift in sedimentary facies from a condensed section of bioturbated Holmehus/Østerrende Fm. clay, into the dark, laminated clays of the Stolleklint Clay (Figs. 3, 4; Heilmann-Clausen et al., 1985; Schoon et al., 2015). A thin glauconitic silt unit (−24.61 to −24.55 m in Figs. 4, 5) marks the boundary, indicating a period of very slow sedimentation (Heilmann-Clausen et al., 1985). Although the boundary is poorly exposed at Fur, the glauconitic silt is likely underlain by an unconformity (∼ −24.6 m in Fig. 5; King, 2016; Schmitz et al., 2004). The PETM is identified just above the base of the Stolleklint Clay by a 4–8‰ negative CIE and appearance of the diagnostic dinoflagellate *Apectodinium augustum* (Jones et al., 2019; Schmitz et al., 2004; Schoon et al., 2015). The Stolleklint Clay grades upward into the ∼60 m thick diatomite-rich Fur Fm. (Figs. 2b, 3, 4). More than 180 ash layers up to 20 cm thick are interbedded in the stratigraphy, with the majority (∼140) found within the Fur Fm. (Figs. 3, 4). The volcanic ashes are grouped into a negative and positive ash series (Larsen et al., 2003), with additional ash layers (termed SK1, SK2, and SK3) within the base of the Stolleklint Clay (Figs. 4, 5). All of the ashes are sourced from NAIP explosive volcanism (Larsen et al., 2003), and distributed throughout the North Sea and Northern Europe (Larsen et al., 2003).

2.1.2. Sampling

This study focuses on the Stolleklint beach locality (Fig. 2a). Here, the PETM was identified just above the base of the Stollek-

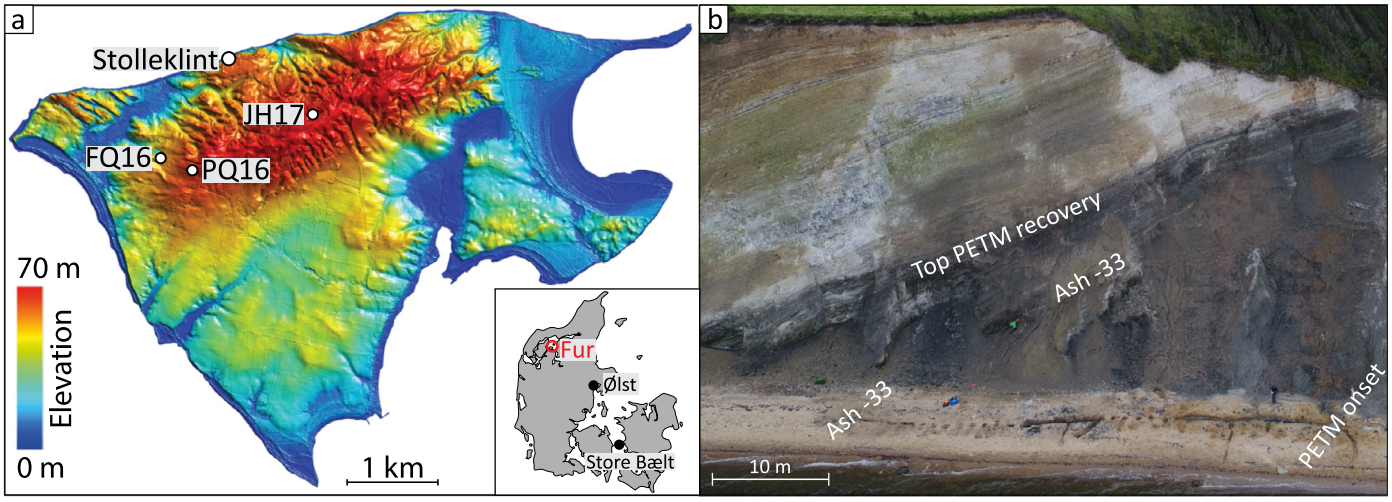

Fig. 2. a) Topographic map of the island of Fur. Samples are from four marked localities: the main locality Stolleklint (56°50′29″N, 8°59′33″E), the quarries near Fur Camping (FQ16 at 56°49′51″N, 8°58′45″E and PQ16 at 56°49′48″N 8°59′07″E), and Jenshøy (JH17; 56°50′05″N 9°00′31″E). The high topography in the north of the island is a partially overturned anticline of Fur Fm. and upper Stolleklint Clay strata. Map courtesy of Egon Nørmark. b) Photo of the Stolleklint beach from the sea, with the PETM indicated. The boundary between the Stolleklint Clay and Fur Fm. is at Ash −33, followed by a gradual transition from clay to diatomite. The inclined bedding is due to the glaciotectonic folding. Note the 43 m long trench along the beach.

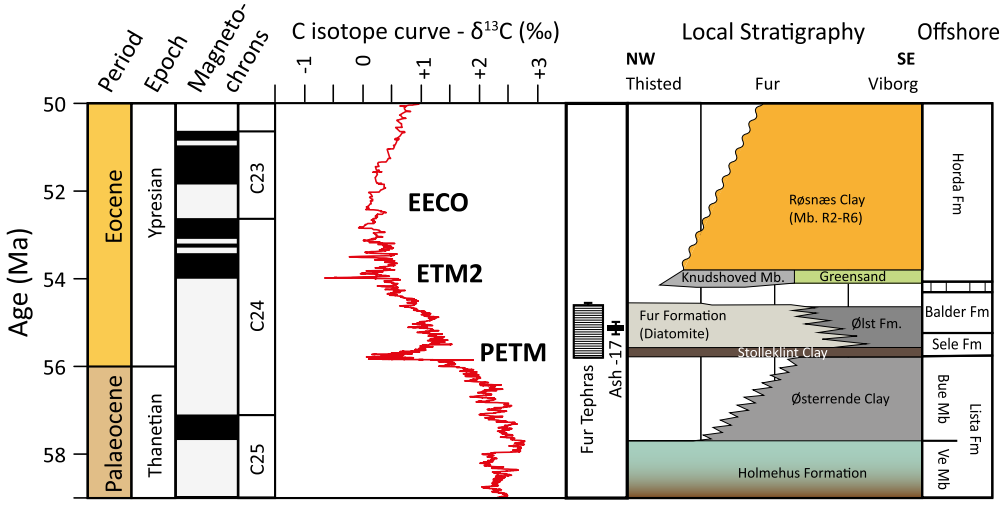

Fig. 3. Composite figure of the Paleocene-Eocene interval, indicating both the local Danish stratigraphy and the correlative offshore North Sea stratigraphy in relation to the PETM and other intervals of environmental change during the Palaeogene. Local stratigraphic section courtesy of Claus Heilmann-Clausen, offshore correlation adapted from King (2016). Carbon isotope data from Cramer et al. (2009) and Littler et al. (2014) and plotted on the GTS2012 timescale (Ogg, 2012). PETM = Paleocene-Eocene Thermal Maximum; ETM2 = Eocene Thermal Maximum 2; EECO = Early Eocene Climatic Optimum.

lint Clay, while Ash −33 marks the end of the CIE body, and Ash −21 the final end of recovery (Jones et al., 2019). The sediments at Fur have experienced very little consolidation and lithification, leaving them soft and easy to sample. Recent glaciotectonic activity has created abundant small-scale folding and thrusting, although only one fault has been identified at Stolleklint, causing a doubling of Ash −33 (Fig. 4). High-resolution sampling was conducted throughout the section by combining samples from three different localities. The main locality is the Stolleklint beach (56°50′29″N, 8°59′33″E; Fig. 2a). Here, a 43 m long and 0.5 m deep trench was excavated (Fig. 2b) in order to reach the base of the Stolleklint Clay and the uppermost Holmehus/Østerrende Fm., which is otherwise poorly exposed. Jones et al. (2019) used careful trigonometry to estimate a local Stolleklint Clay thickness of 24.4 ± 2 m (24.2 m excluding ash layers) from the base of Ash SK1 to the base of Ash −33. The lowermost part of the trench was sampled every cm from ∼25 cm below to ∼90 cm above Ash SK1, recovering the entirety of the CIE onset. The remainder of the trench up to Ash −33 was sampled every 0.5 m (0.2–0.3 m estimated local thickness). Samples from the CIE recovery and lower post-PETM stratigraphy were collected from the cliff face at Stolleklint (Fig. 2b) and from quarries near Fur Camping (FQ16 at 6°49′51″N, 8°58′45″E and PQ16 at 56°49′48″N 8°59′07″E; Fig. 2a). Samples from Ash +1 upwards were collected from the quarry at Jenshøy (JH17; 56°50′05″N 9°00′31″E; Fig. 2a).

2.2. Analytical methods

2.2.1. Carbon isotopes

Analyses of total organic carbon (TOC) and stable carbon isotopes of bulk samples ($\delta^{13}C_{TOC}$) from Ash −11 and up were conducted at the Jahren Lab at the University of Oslo. Powdered samples were decalcified using 1M HCl, then oven-dried at 50 °C and re-homogenised. About 8 mg of decalcified sample was sealed in tin capsules and loaded into a Costech Analytical Zero-Blank Autosampler. Organic $\delta^{13}C_{TOC}$ measurements and TOC concentrations

were analysed using a Thermo Fisher Scientific Flash Elemental Analyzer, coupled with a Thermo Fisher Scientific DeltaV Isotope Ratio Mass Spectrometer. Reproducibility of TOC and $\delta^{13}C_{TOC}$ was better than 0.01 wt% and 0.06‰, respectively. Previously published $\delta^{13}C_{TOC}$ and TOC analyses from the base of the section up to Ash −13 from Jones et al. (2019) are included.

2.2.2. Molecular extraction and fractionation

Crushed samples (1 g) were extracted using a Thermo 350 Accelerated Solvent Extractor with the following program: preheat = 5 min; heat = 5 min; static = 5 min; pressure = 10.34 MPa; flush = 70%, purge = 300 s.; cycles = 3; solvent = 9:1 dichloromethane:methanol. Solvent extracts were reduced to dry with a Genevac EZ-2 vacuum centrifuge. Total lipid extracts were quantified gravimetrically before column fractionation. Aliquots of the total lipid extracts were loaded onto small silica gel columns and fractions were eluted with hexane, hexane:dichloromethane (4:1), and dichloromethane:methanol (1:1) yielding the nonpolar, aromatic, and polar fractions, respectively.

2.2.3. GC- and LC-MS analysis

Aliphatic and aromatic fractions were desulphurised using copper beads, before being analysed for biomarker identification using a Thermo Trace 1310 gas chromatograph coupled to a Thermo TSQ8000 mass spectrometer at the National Oceanographic Centre, Southampton. The gas chromatograph used DB-5 column (30 m × 0.25 mm i.d, 0.25-µm film thickness). The oven program was started at 40 °C (held for 2 min), increased at a rate of 6 °C/min to 310 °C, and then held for 20 min. GC-MS analyses of the aliphatic and aromatic fractions generally yield low concentrations of biomarkers, with the *n*-alkanes and related compounds of m/z = 57 being the most abundant throughout. Compound identification of *n*-alkanes and pristane/phytane was made using mass spectra, library matches, and comparisons to known standards.

The polar fraction containing GDGTs was re-dissolved in hexane:isopropanol (99:1) and filtered with a 0.45 micron PTFE filter. The GDGTs were analysed on an Agilent 1260 Infinity HPLC coupled to an Agilent 6120 single quadrupole mass spectrometer at the University of Arizona, using two BEH HILIC silica columns (2.1 × 150 mm, 1.7 µm; Waters) and the improved chromatographic methodology of Hopmans et al. (2016). We calculated peak areas using the MATLAB package software ORIGAmI (Fleming and Tierney, 2016).

2.2.4. TEX_{86} values and calibration

TEX_{86} values were calculated from isoprenoid GDGT (isoGDGT) peak areas according to Schouten et al. (2002), yielding values that are all within the calibration range in modern oceans (0.3 to 0.8; Fig. 4), suggesting that no extrapolation is required (Hollis et al., 2019). Several calibrations for estimating SSTs from TEX_{86} values have been developed, based on extensive modern global core-top datasets. The earliest calibration by Schouten et al. (2002) used a linear relationship, which has since been shown to correlate poorly in temperatures <5 °C and in some extreme settings such as the Red Sea (e.g. Kim et al., 2010). Other calibrations have been developed to circumvent this, such as the exponential calibration TEX^H_{86} (Kim et al., 2010), which excludes Red Sea data and temperatures below 10 °C. However, recent studies show that TEX^H_{86} has a statistical bias (regression dilution) that results in systematic underestimation of temperatures at high TEX_{86} values (Tierney and Tingley, 2014). Based on the recommendations of the DeepMIP model comparison project (Hollis et al., 2019), the use of TEX^H_{86} is no longer recommended for SST determinations in warm greenhouse climates. We refer readers to Hollis et al. (2019) for a full discussion of the limitations of TEX^H_{86} and recommendations for temperature estimates in the PETM and early Eocene intervals.

Following DeepMIP recommendations, we apply the Bayesian regression model BAYSPAR (Tierney and Tingley, 2014) to convert TEX_{86} values to SSTs. The linear BAYSPAR calibration varies its regression terms spatially, taking into account the regional differences in the relationship between SST and TEX_{86} that are observed today (Tierney and Tingley, 2014). BAYSPAR also includes modern Red Sea data, which is likely a strength as Red Sea-type distributions are commonly observed in PETM and early Eocene sites (Hollis et al., 2019). However, for deep-time applications, BAYSPAR is run in analogue mode, which does not use regionally specific calibration parameters. Rather, analogue mode uses all regression parameters associated with TEX_{86} values within a specified threshold of the data, regardless of location. We applied BAYSPAR to infer SST with the following settings: prior mean = 20, prior standard deviation = 10, TEX_{86} tolerance = 0.15, number of iterations = 2500. As TEX^H_{86} has been applied to other PETM sites, the TEX^H_{86} calibration can be found in the Supplementary data for comparative use.

2.2.5. Other biomarker indices

There are several caveats and overprinting factors that can potentially bias TEX_{86} values, particularly through the addition of isoGDGTs that are not produced by Thaumarchaeota in the upper water column. Several methods are applied to assess the potential bias of TEX_{86} values. The Branched and Isoprenoid Tetraether (BIT) index measures the relative input of terrestrially derived branched GDGTs (brGDGT) and the marine-derived crenarchaeol. BIT was calculated following Hopmans et al. (2004). BIT values above 0.4 may indicate that TEX_{86} temperatures are compromised by terrestrially derived isoGDGTs (Weijers et al., 2006). However, there is no universal cut-off for BIT values as BIT does not straightforwardly relate to terrestrial organic matter (OM) fluxes and brGDGTs can also be produced *in situ* in marine environments (e.g. Peterse et al., 2009).

The Methane Index (MI) assess the potential influence of methanotrophic and methanogenic GDGT producers, which can bias TEX_{86} values (Zhang et al., 2011). MI values >0.5 characterise sedimentary conditions with a substantial methanogenic influence, typically in anoxic basins or near methane seeps (Zhang et al., 2011). Methanogenic archaea can also synthesise GDGT-0 (Blaga et al., 2009). The ratio GDGT-0/Crenarchaeol has been suggested as an indicator of methanogenesis on the isoGDGT population, with a substantial contribution indicated by values >2 (Blaga et al., 2009). The delta-ring index (ΔRI; Zhang et al., 2016) detects whether the isoGDGT distributions differ from the surface calibration dataset. It can indicate if factors other than temperature are controlling the GDGT distribution, often detecting anything that would otherwise be flagged by BIT and MI. ΔRI is calculated by comparing the temperature dependent Ring Index (RI) and TEX_{86} to the modern global TEX_{86}-RI relationship, with an upper limit of |0.3| (95% confidence interval of the modern regression). TEX_{86} derived SSTs where BIT values are >0.4 are shown as open circles (Figs. 4, 5). All samples where ΔRI exceeds |0.3| also have BIT>0.4, and have been marked red in Figs. 3 and 4. All marked samples should be interpreted with some care.

Additional environmental constraints are indicated by biomarker proxies from the aliphatic fraction analysed with GC-MS. The Terrigenous Aquatic Ratio (TAR; Peters et al., 2005) is a proxy of potential terrigenous input relative to marine. It is defined as the ratio of the primarily land-plant derived long-chain *n*-alkanes nC_{27}, nC_{29} and nC_{31}, over the short-chain *n*-alkanes nC_{15}, nC_{17} and nC_{19} mainly derived from marine algae. Pristane and phytane are derived from the phytol side-chains of chlorophyll in algae and bacteria. These can be used as a proxy for both source region and redox conditions. Reducing conditions promote the reduction of phytol to phytane, while oxic conditions leads to oxidation of phytol to pristane (Peters et al., 2005).

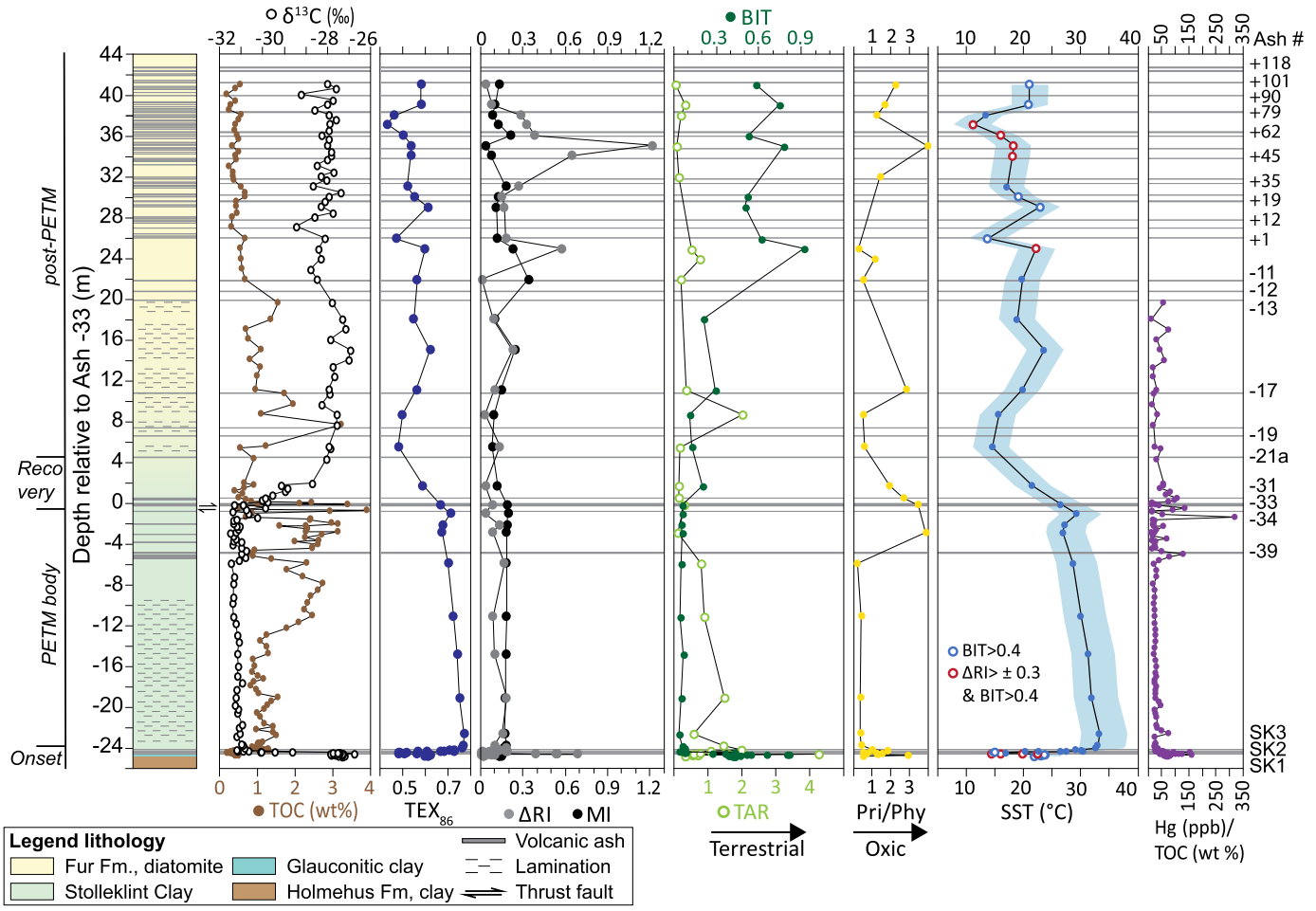

Fig. 4. Composite data from the island of Fur, combining samples from Stolleklint beach and three nearby quarries. Data includes $\delta^{13}C$ and TOC analyses, TEX_{86} values, BAYSPAR calibrated TEX_{86} SSTs with 1σ errorbars indicated by blue area, several organic biomarker ratios, and mercury/TOC from Jones et al. (2019). Hg values are included in the Supplementary data. Composite log of the local lithology and its relation to the interpreted PETM-onset, -body and -recovery, and post-PETM sections shown on the left. Grey lines indicate ash layers, with the ash stratigraphy indicated on the right. Legend shown at the base. TOC = Total Organic Carbon; SST = Sea Surface Temperature; ΔRI = Ring Index; MI = Methane Index; BIT = Branched and Isoprenoid Tetraether index; TAR = Terrigenous Aquatic Ratio; Pri/Phy = Pristane/Phytane.

3. Results and discussion

3.1. Shape and duration of the PETM at Fur

The Fur stratigraphy is an outstanding locality, comprising an uninterrupted PETM section of well-preserved marine clays. GC-MS measurements show that the *n*-alkanes have a constant high odd-over-even preference (OEP; Supplement), with OEP >1 throughout indicating that the whole sequence is thermally immature and well suited for organic geochemical analyses (Peters et al., 2005).

The late Paleocene Holmehus/Østerrende Fm. show stable $\delta^{13}C_{TOC}$ values around −26‰, and TOC concentrations of ∼0.5 wt% (Figs. 4, 5). The C25r-C25n boundary (∼57.7 Ma; Ogg, 2012) marks the top of the Holmehus Fm., but the duration of the overlying unconformity is undefined as it is unclear how much of the overlying Østerrende Fm. is present at Fur (Fig. 3; King, 2016). The $\delta^{13}C_{TOC}$ values in the overlying glauconitic unit remain stable at ∼ −26‰ while TOC values drop to about 0.3 wt%. Neither the age nor duration of the glauconitic silt is well constrained, although it is most likely a part of the basal section of the Stolleklint clay, similar to that described at Ølst ∼80 km to the southeast (Fig. 2; King, 2016; Schmitz et al., 2004). The glauconitic layer is ∼5 m thick at the Store Bælt section but only ∼5 cm thick at Ølst and Stolleklint (Fig. 2; Schmitz et al., 2004; Schoon et al., 2015), suggesting that it is highly condensed. An interstitial clay (between ashes SK1 and SK2) with ∼0.4 wt% TOC is found above the glauconitic silt prior to the PETM onset (Figs. 4, 5).

The PETM onset is defined by a sharp CIE of ∼−4.5‰ (from −26.5 to −31‰) immediately above Ash SK2, which is larger than average bulk marine OM records (McInerney and Wing, 2011). The CIE onset at Fur was concordant with the sudden dominance of the subtropical dinoflagellate *Apectodinium augustum* (Heilmann-Clausen et al., 1985; King, 2016). A pronounced increase in TOC from 0.45 to 1.5 wt% and a shift from bioturbated to laminated clays occur ∼2 cm above the CIE onset (Figs. 4, 5), suggesting a shift to anoxic conditions. TOC concentrations remain relatively stable for the first half of the CIE body, before increasing up to 3.9 wt% in the upper half (Fig. 4). This large increase in TOC is followed by a shift from dark laminated clays to massive, black clays with abundant pyrite suggesting a highly anoxic environment. Just above Ash −33 at the start of the CIE recovery, TOC concentrations drop to <1 wt%.

The CIE body is defined by an extended interval (∼24 m) of sustained stable negative $\delta^{13}C_{TOC}$ values (Fig. 4). In contrast, the recovery phase is relatively sharp, starting at Ash −33 and returning to pre-PETM values by Ash −21 (∼4.5 m thick; Fig. 4). The small thrust fault that cuts across Ash −33 in parts of the Stolleklint beach section likely leads to some uncertainty about the exact shape and duration of the $\delta^{13}C_{TOC}$ curve during the shift from CIE body to recovery (Fig. 4). The unusually thick CIE body at Fur most

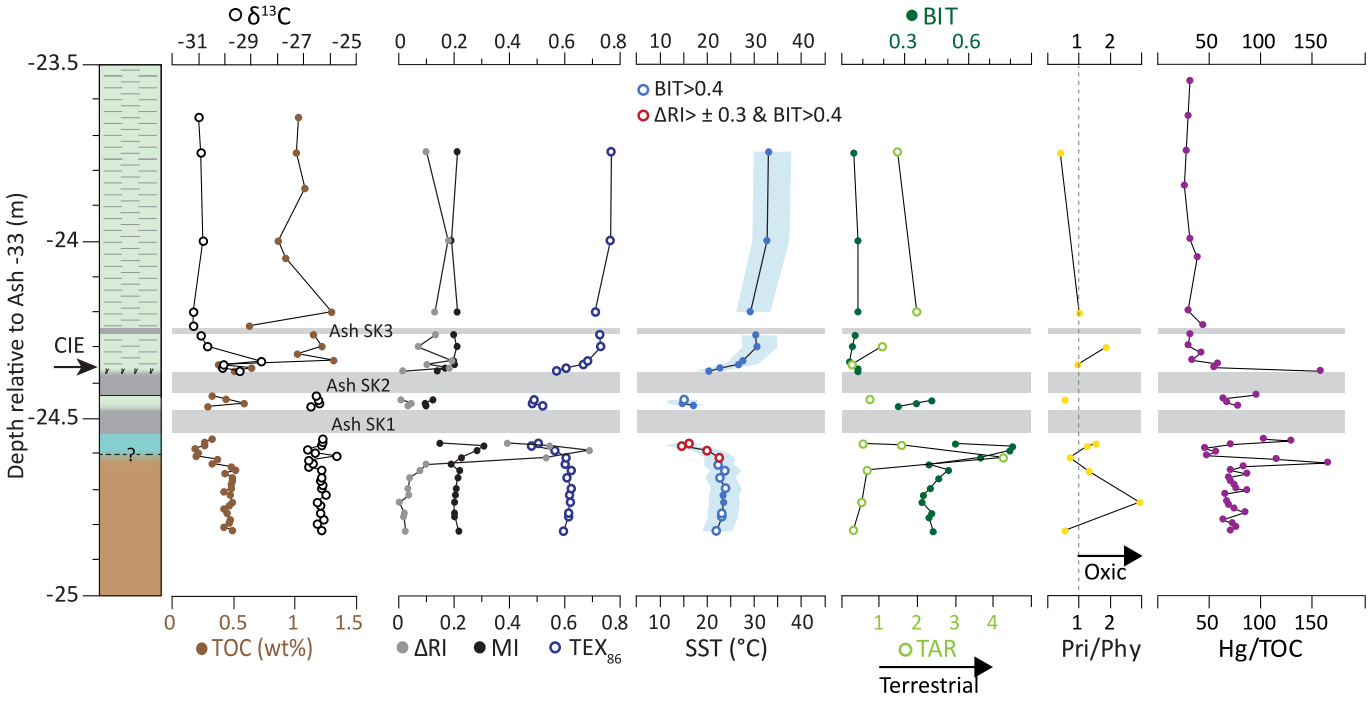

Fig. 5. Zoom-in of Fig. 4 showing data covering the PETM onset at Fur. Samples from the base of Stolleklint beach. Data include $\delta^{13}C$ and TOC analyses, TEX_{86} values, BAYSPAR calibrated TEX_{86} SSTs with 1σ errorbars indicated by blue area, several organic biomarker ratios, and mercury/TOC from Jones et al. (2019). Composite log of the local lithology and its relation to the interpreted PETM-onset shown on the left. Grey bands indicate ash layers SK1, SK2, and SK3. Legend shown in Fig. 4. TOC = Total Organic Carbon; SST = Sea Surface Temperature; ΔRI = Ring Index; MI = Methane Index; BIT = Branched and Isoprenoid Tetraether index; TAR = Terrigenous Aquatic Ratio; Pri/Phy = Pristane/Phytane.

likely reflects a large increase in sedimentation rates during the PETM CIE that wanes again during the recovery. Jones et al. (2019) estimated a 24.2 m ash-free thickness of the CIE body at Stolleklint. If we assume a 100 kyr for the PETM body (van de Meulen et al., 2020), the sediment accumulation rate for the Stolleklint Clay is about 24 cm/kyr (24.2 m/100 kyr). Considering the condensed and bioturbated nature of the underlying glauconitic silt, this indicates a considerable increase in sedimentation rate. The increasingly diatomite-dominated lithology suggests a decreasing sedimentation rate during the CIE recovery and post-PETM sections.

The post-PETM period section is characterised by $\delta^{13}C_{TOC}$ values that fluctuate between −26 and −28‰ (Fig. 4), typical for bulk marine OM records at this time (McInerney and Wing, 2011). The lower, laminated part of the post-PETM section (∼ + 4 to +20 m in Fig. 4) is composed of a relatively clayey diatomite showing variable TOC concentrations (0.5 to 3.2 wt%). In contrast, the uppermost ∼20 m of the stratigraphy, comprised almost entirely of diatomite, has stable low concentrations around 0.5 wt% TOC. The age control on the post-PETM Fur Fm. is limited as only the post-PETM Ash −17 is so far radioisotopically dated (Storey et al., 2007a), with a recalibrated Ar-Ar age of 55.6 ± 0.12 Ma (Jones et al., 2019). Westerhold et al. (2009) estimated a 200 kyr duration between Ash −17 and +19, placing Ash +19 at about 55.4 Ma (Fig. 6) and a total 300 kyr duration of the positive ash series. Stratigraphic correlations with the lower Balder Fm. places the top of the Fur Fm. at ≥ 54.6 Ma (King, 2016), prior to the onset of the Eocene Thermal Maximum 2 (ETM 2; Fig. 3).

3.2. Constraining PETM temperature changes

3.2.1. Apparent late Paleocene cooling

The late Paleocene interval comprises the lowermost ∼65 cm of the stratigraphy (Figs. 4, 5). The Holmehus/Østerrende Fm. is characterised by relatively stable SSTs around ∼23 °C (Fig. 5). BAYSPAR calibrated SSTs drop down to a minimum of 14.5 ± 3[1σ] °C ∼2 cm below Ash SK1 (Fig. 5), corresponding to a SST drop of ∼8 °C (Fig. 5). This corroborates the preliminary findings of Schoon et al. (2015), who found evidence of a pre-PETM cooling event from two samples at Stolleklint. However, the age of the late Paleocene strata below SK2 is poorly constrained. While there is no compelling evidence for hiatuses within the sediments above the glauconitic unit, considering the bioturbation in these sediments we cannot rule one out either. The timing of the cooling is therefore late Paleocene (<57.7 Ma; King, 2016), although it could be just prior to the onset of the PETM.

This apparent cooling interval can be divided in two, with the lower part found in the glauconitic silt below Ash SK1 and the upper in the interstitial clay between Ashes SK1 and SK2. The entire cooling interval is characterised by low abundances of the Crenarchaeol isomer (Cren'; Supplement), suggesting a slightly different Thaumarchaeota population in this interval. The cooling onset coincides with increases in several overprinting signals that can bias TEX_{86} values (Fig. 5; Supplement). Firstly, ΔRI increases sharply and exceeds threshold values of |0.3| at the start of the cooling, suggesting non-thermal factors likely control the GDGT distribution (Zhang et al., 2016). Both MI and GDGT-0/Crenarchaeol are elevated in the same interval (MI up to 0.3, GDGT-0/Cren up to 1.9; Fig. 5; Supplement) suggesting potential methanogenic influence (Blaga et al., 2009; Zhang et al., 2011). An abrupt increase in TAR (from 0.7 to 4.3) and BIT (up to 0.8) in the base of the glauconitic silt suggests a large increase in terrestrial input influencing TEX_{86} values (Fig. 5; Peters et al., 2005; Weijers et al., 2006). Preferential degradation of isoGDGTs due to oxic degradation could also have an influence, potentially resulting in increased BIT values and lower absolute temperatures (Hopmans et al., 2004). Bioturbation, low TOC concentration, and pristane/phytane partly >1 indicate relatively oxygenated conditions below Ash SK1 (Fig. 5).

Low TEX_{86} values and inferred cooling continues in the upper part between Ashes SK1 and SK2. While the upper part is slightly

affected by elevated BIT values (from 0.27 to 0.43; Fig. 5), ΔRI decreases below threshold values and there is no compelling evidence of methanogenic influence (Fig. 5; Supplement). Despite the elevated BIT values, the low ΔRI suggests that the TEX_{86} values are likely to be robust. Schoon et al. (2015) observed a similar cooling in mean annual air temperatures (MAAT) from this interval, reconstructed from soil-derived brGDGTs. While brGDGTs may be produced *in-situ* (e.g. Peterse et al., 2009) and offset MAAT estimates, a separate corroborating proxy could support the presence of a cooling event before the CIE onset. Inglis et al. (2019) also describe a terrestrial cooling during the PETM onset in England, although they argue strongly that this is due to caveats with the brGDGT palaeothermometer. The presence of a cooling before the CIE is at odds with most other PETM sections, where temperatures are either stable (e.g. Sluijs et al., 2006) or even show a pre-CIE warming (Frieling et al., 2019). It is possible that the absence of any pre-PETM warming at Fur could be due to a regional cooling event affecting the North Sea. The interval between Ashes SK1 and SK2 is unlikely to be adversely affected by TEX_{86} bias, suggesting that the cooling observed is a real feature. However, the numerous overprinting factors and missing/condensed stratigraphy in the lower glauconitic silt indicates that more work is needed to constrain the likelihood and duration for such a cooling event.

3.2.2. PETM warming and recovery

The PETM onset, body and recovery show consistently low ΔRI, MI, and BIT indices, indicating TEX_{86} values are likely unbiased. While BIT values are consistently low (<1) throughout the CIE body, changing TAR values indicating variable input of long-chain *n*-alkanes from terrigenous sources during the PETM (Fig. 4). The ∼−4.5‰ CIE marking the PETM onset at Fur is followed closely by a SST increase to about 30 °C (Fig. 5). Maximum PETM SSTs of 33.3 ± 4 [1σ] °C is reached only ∼1.8 m above the CIE onset (Figs. 4, 5), suggesting a relatively rapid temperature response to carbon release. The temperature increase at Fur represents a minimum estimate of 10 °C warming from late Paleocene values (Figs. 4, 5). The TEX_{86}^{H} calibration is within the 1σ calibration error of BAYSPAR, and shows the same relative trend with lower maximum and higher minimum SST's resulting in a minimum 7 °C PETM warming (Supplement). A 7–10 °C SST warming is at the upper end of previous estimates for the PETM (Dunkley Jones et al., 2013; Frieling et al., 2017), although it is important to note that TEX_{86} typically yield slightly higher SSTs than other proxies (e.g. Inglis et al., 2020). The warming agrees relatively well with other mid-latitude shelf settings (Frieling et al., 2014; Zachos et al., 2006) and the Southern Ocean (Sluijs et al., 2011), but is higher than those observed in the Tropics (Frieling et al., 2017), the Arctic (Sluijs et al., 2006), and deeper mid-latitude settings (e.g. Bay of Biscay; Bornemann et al., 2014). However, spatial variability of warming and high latitude amplification have been described both from modelling and proxy studies during the PETM (Dunkley Jones et al., 2013; Frieling et al., 2017). The estimated temperature increase and estimated maximum PETM SSTs also agrees well with recently modelled Global Mean Surface Temperature for the PETM of 33 °C and a temperature increase of 4–9 °C from latest Paleocene (Inglis et al., 2020).

The negative $\delta^{13}C_{TOC}$ values are near constant throughout the PETM body phase until Ash −33 (Fig. 4), indicating continued input of depleted carbon and little change to the carbon isotope composition of the surface carbon reservoir. However, after reaching maximum SSTs shortly after the onset, temperatures decline throughout the remainder of the PETM and return to late Paleocene values by the end of the CIE recovery (Fig. 4). This suggests that negative feedback mechanisms lowering temperatures were active during the PETM, such as increased silicate weathering and OM burial, removing CO_2 from the atmosphere (McInerney and Wing, 2011). Sedimentation rates increase at Fur and globally during the PETM, reflecting enhanced weathering in response to a stronger hydrological cycle (Kender et al., 2012). Increased productivity and OM burial in shelf settings has also been demonstrated globally (Ma et al., 2014), and likely had an important role in atmospheric carbon drawdown (e.g. Gutjahr et al., 2017). John et al. (2008) suggested that due to drastically increased sedimentation rates and productivity during the PETM, mid-latitude shelves became highly efficient sinks for organic carbon burial. The substantial increase in sedimentation rate during the PETM and in OM burial in the upper half of the CIE body at Fur (Fig. 4), corroborates the important role for shelves in carbon drawdown and the final PETM CIE recovery.

3.3. Post-PETM temperature variations

Temperatures drop during the CIE recovery to a minimum of 15 ±3[1σ] °C, 1 m above Ash −21a. An initial increase in SSTs up to 23.6 ± 3.3 [1σ] °C (+15 m in Fig. 4) is followed by varying SSTs (11–23 °C) during the post-PETM (Fig. 4). While the lower 15 m have low ΔRI, MI, and BIT indices indicating relatively robust TEX_{86} values, the upper 25 m are characterised by a number of overprinting factors. ΔRI values are high and exceeding |0.3| in several samples, suggesting non-thermal factors are controlling isoGDGT distribution (Zhang et al., 2016). High BIT ratios prevail, with values >0.4 for all samples above +21 m height (Fig. 4). This may reflect inclusion of soil derived branched GDGTs (Hopmans et al., 2004; Weijers et al., 2006), although low TAR values suggest this section is dominated by marine-sourced short-chain *n*-alkanes (Fig. 4; Peters et al., 2005). Concentrations of brGDGTs are also low and sometimes below detection limit in the post-PETM section (Fig. 4; Supplement), which may compromise BIT values. Alternatively, the high BIT ratios could reflect preferential oxic degradation of marine isoGDGTs. This is supported by the low TOC concentrations and high pristane/phytane ratios (Fig. 4). While MI values are all <0.3 (Figs. 4, 5), the GDGT-0/Crenarchaeol ratio is relatively high in several samples post-PETM (>2 at ∼ +35 m height; Supplement), suggesting a potential for limited methnogenesis (Blaga et al., 2009).

Although there are many possible factors affecting TEX_{86} values, the general trend of lower post-PETM temperatures is likely to be a real feature. The Fur Fm. was deposited during a ∼1 Myr period before 54.6 Ma (King, 2016), thus predating ETM2 and the Early Eocene Climatic Optimum (Figs. 3, 6). Global temperatures show a general cooling after the PETM (Cramwinckel et al., 2018; Frieling et al., 2017; Inglis et al., 2020), although the post-PETM SSTs at Fur seem anomalously low compared to similar mid-latitude sites (Frieling et al., 2014; Bornemann et al., 2014). This is particularly true for the lowest SSTs recorded just above the CIE recovery (15 ± 3 [1σ] °C at +5.5 m in Fig. 4), where potential TEX_{86} bias is least. A diversity reduction in plant communities in the Shetland basin has also been inferred to indicate lowered surface temperature in the period between the PETM and the ETM2 (Jolley and Widdowson, 2005). It is therefore possible that regional conditions led to enhanced cooling in the Danish region and possible larger parts of the Northeast Atlantic.

3.4. The role of North Atlantic Igneous Province volcanism

The NAIP is known to have been particularly active across the PETM. The dominant mode of eruption was effusive, building up huge continental flood basalts in Greenland and the Faroe Islands (Fig. 2). Constraints on timing and duration of the East Greenland lavas suggest that a 5–6 km thick lava pile was emplaced between 56.0 and 55.6 Ma (Jones et al., 2019; Larsen and Tegner, 2006). However, there is currently no data on whether these eruptions

were continuous, pulsed, or constrained to a much shorter time window. This has significant implications for the NAIP as a potential climate forcing. The main climatic impact of large eruptions is cooling, caused by sulphuric acid aerosols in the atmosphere increasing the planetary albedo (Robock, 2000). Atmospheric residence times for sulphur depend on whether it reaches the stratosphere (1–3 yr), or if it is released to the troposphere (weeks). This means that dominantly tropospheric emissions would result in a more regionally constrained cooling. A historic example is the 1783-84 eruption of Laki (Iceland) that caused a 2–3 yr of cooling largely constrained to the northern hemisphere (Thordarson and Self, 2003). However, the limited residence time of sulphur in the atmosphere restricts the duration of climatic impact to essentially syn-eruptive (Jones et al., 2016), which means transient cooling events from rapid explosive eruptions would not be preserved in the palaeotemperature record. Modelling has shown that the global climate can recover from perturbations during large effusive eruptions (4–6 °C cooling) within 50 yr of the eruption end (Schmidt et al., 2016). Therefore, the only potential method of preserving volcanic cooling in sedimentary sequences would be near-continuous eruptions over several centuries. The duration of periods of quiescence between eruptions is therefore a particularly important factor.

The hundreds of ash layers preserved in North Sea sediments indicate widespread explosive volcanism associated with the NAIP (Larsen et al., 2003). However, explosive eruptions are typically a minor volumetric component of LIPs. The unusual prevalence of basaltic tephra suggests that the explosiveness of eruptions was enhanced by magma-seawater interaction as Greenland and Eurasia broke apart (Larsen et al., 2003). Therefore, the increase in ash layers in the upper parts of the Fur stratigraphy likely reflect a change in eruptive style, rather than an increase in total volcanism. The positive ash series follows a period of long-lasting effusive flood basalt eruptions, which typically do not produce large amounts of ash, but do provide a constant supply of sulphur and other volcanic gases. While the volcanic ash layers mainly reflect periods of explosive volcanic activity, Hg/TOC anomalies indicate both the explosive and effusive activity.

Evidence from the Danish stratigraphy suggests at least four episodes of enhanced NAIP volcanism (Fig. 6). The first period occurs in the late Paleocene prior to the PETM onset, and is indicated by Hg/TOC anomalies (Jones et al., 2019) and the deposition of Ashes SK1 and SK2 (Figs. 5, 6). This period of prolonged and enhanced volcanic activity prior to the PETM onset coincides with the TEX_{86} derived apparent cooling (Figs. 5, 6). Active NAIP volcanism is corroborated in the pre-PETM strata in Svalbard, where large Hg/TOC anomalies have been documented (Jones et al., 2019), together with low $^{187}Os/^{188}Os$ values suggesting weathering of substantial volumes of basaltic material (Wieczorek et al., 2013). The North Sea Basin is ideally placed to record potential volcanic cooling due to its close proximity to the NAIP and being downwind of the easterly polar jet stream. If effusive volcanism led to largely tropospheric degassing, then the surface cooling would be most prominent in the North Sea area and potentially absent from distal records, particularly in the tropics and southern hemisphere.

It is important to note that volcanic activity is one of several factors that could potentially explain the available SST proxy data. Thermal uplift from the NAIP led to the isolation of the North Sea during the latest Paleocene and earliest Eocene (Knox et al., 2010), which would have changed the oceanographic conditions. This could have affected the degree of mixing and therefore heat transport in the North Sea basin, potentially leading to slightly cooler SST conditions in the late Paleocene. A bolide impact has been identified at the Paleocene-Eocene transition that may have cooled surface temperatures through impact ejecta (Schaller et al., 2016). However, no indices of such an event have been found in

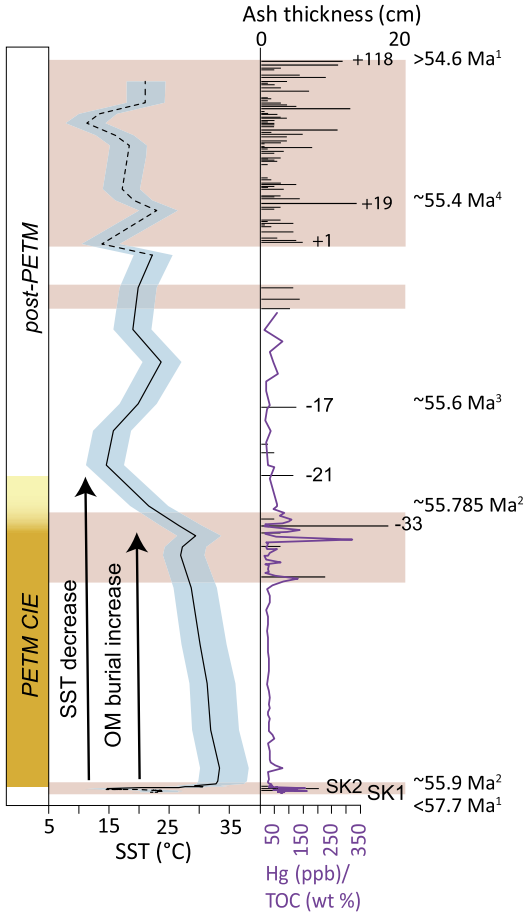

Fig. 6. Summary of temperature changes and volcanic proxies. Red bands show periods of active NAIP volcanism as indicated by high ash accumulation and Hg/TOC anomalies. Yellow band indicates duration of the PETM carbon isotope excursion (CIE). Black line shows BAYSPAR calibrated Sea Surface Temperatures (SST), where blue band indicates the associated 1σ error, and dashed line SSTs with high potential TEX_{86} bias. OM = Organic Matter; TOC = Total Organic Carbon; [1]King (2016); [2]Charles et al. (2011), assuming the timings of the Svalbard and Fur CIEs are coeval; [3]Storey et al. (2007a); [4]Westerhold et al. (2009).

Denmark (Schmitz et al., 2004) and the impact is placed at the CIE onset (Schaller et al., 2016), thereby post-dating the apparent cooling. If the observed cooling is a true indication of palaeotemperatures, then the most plausible explanation is that NAIP volcanism led to a regional cooling in the late Paleocene before the CIE onset in the interval between Ashes SK1 and SK2 (Fig. 5). However, temperature reconstructions from other areas proximal to the NAIP are sparse. More work is needed around the northeast Atlantic margins to confirm whether the apparent cooling is real, its exact timing and duration, and to constrain the potential regional distribution of cooling.

There is no compelling evidence for enhanced volcanism during most of the PETM body in the Danish strata (Fig. 6). This is noteworthy as the ~100 kyr CIE body interval occurs during the ~400 kyr (56.0–55.6 Ma) interval known for elevated NAIP volcanism (Gutjahr et al., 2017; Larsen and Tegner, 2006). This includes the important phase of sill emplacement and thermogenic degassing through hydrothermal vent complexes (Svensen et al., 2004; Frieling et al., 2016). The available proxies from Fur do not shed light on the timing nor duration of the thermogenic degassing phase of the NAIP. The cooling during the PETM recovery is coincident with the re-emergence of thick ash layers and Hg/TOC anomalies (Fig. 6). Temperatures decrease >10 °C during the CIE recovery (Fig. 4), and the abundance of volcanic proxies in the Danish strata toward the end of the CIE body and into the CIE recovery suggests

that the effects of volcanism (e.g. sulfate aerosols, weathering) may also have contributed to the cessation of hyperthermal conditions. The >140 ash layers present in post-PETM strata indicate intense and long-lasting explosive volcanism (Figs. 4, 6). These periods of enhanced volcanic activity coincide with the TEX_{86} derived cool SSTs (Figs. 4, 6). A similar cooling is suggested within the exceptionally ash rich contemporaneous Balder Fm. (Fig. 3) of the Shetland basin (Jolley and Widdowson, 2005). It is possible that the period of exceptionally explosive volcanic activity following the PETM (Fig. 6) led to a period of regionally cooler temperatures in the North Sea and Northeast Atlantic region.

4. Conclusions

A $\sim -4.5‰$ change in $\delta^{13}C_{TOC}$ defines the PETM onset in an expanded section at Fur Island, Denmark. The CIE onset is accompanied by a marked lithological transition from bioturbated to laminated clays and a dramatic increase in both sedimentation rate and OM content. The late Paleocene section shows an apparent SST cooling of up to 8 °C, based on the TEX_{86} proxy. While the large potential for TEX_{86} bias during the first stage make validity of this cooling episode somewhat speculative, the potential TEX_{86} bias decrease substantially suggesting the latest stage may represent a genuine cooling episode. This latest robust stage of apparent cooling coincides with deposition of two major ash layers (SK1 and SK2) and significant Hg/TOC anomalies, suggesting that regional cooling from voluminous volcanism may be the cause of temporally depressed SSTs in the North Sea during the late Paleocene.

TEX_{86}-derived SSTs yield a minimum temperature increase of ~10 °C across the CIE onset, depending on the calibration method used. This temperature increase is within previous estimates for the PETM, though at the upper end. Maximum SST is reached relatively shortly after the CIE onset, followed by a shift to gradually declining temperatures. There is evidence for negative feedbacks to warming, such as silicate weathering and organic matter burial, occurring during the stable body phase of the PETM CIE. SSTs decreased substantially, reaching anomalously low temperatures by the end of the CIE recovery. A re-emergence of volcanic proxies during the end of the CIE body and the CIE recovery, suggest the effects of volcanism may have contributed to the cessation of hyperthermal conditions. During the post-PETM interval, TEX_{86}-derived SSTs are variable and partly anomalously low (11–23 °C). While overprinting factors could affect TEX_{86}-derived SSTs in parts of the stratigraphy, the effect of persistent explosive volcanic activity during this period is likely to have had some effect on SSTs in the North Sea region.

Declaration of competing interest

The authors declare that they have no known competing financial interests or personal relationships that could have appeared to influence the work reported in this paper.

Acknowledgements

We thank reviewer Dr. Peter Bijl, the anonymous reviewer, and editor Dr. Laura Robinson, for their very thorough and constructive comments. Prof. Emeritus Claus Heilmann-Clausen, Dr. Joost Frieling is sincerely thanked for good and helpful discussions. P. Sargent Bray, Bo Schultz, Dr. Sverre Planke, Prof. Christian Tegner, and Dr. Valentin Zuchuat are all warmly thanked for their assistance. This project was supported by the Research Council of Norway's funding schemes "Unge Forskertallenter" project number 263000 (project Ashlantic) and "Centres of Excellence" project number 223272, and their funding to the Norwegian Research School DEEP with project number 249040/F60. J. Whiteside is thankful to support from an Annual Adventures in Research grant. J. Tierney acknowledges support from The David and Lucile Packard Foundation and The Heising-Simons Foundation Grant #2016-015.

Appendix A. Supplementary material

Supplementary material related to this article can be found online at https://doi.org/10.1016/j.epsl.2020.116388.

References

Babila, T.L., Penman, D.E., Hönisch, B., Kelly, D.C., Bralower, T.J., Rosenthal, Y., Zachos, J.C., 2018. Capturing the global signature of surface ocean acidification during the Palaeocene–Eocene Thermal Maximum. Philos. Trans. - Royal Soc., Math. Phys. Eng. Sci. 376 (2130), 20170072.

Blaga, C.I., Reichart, G.J., Heiri, O., Damsté, J.S.S., 2009. Tetraether membrane lipid distributions in water-column particulate matter and sediments: a study of 47 European lakes along a north–south transect. J. Paleolimnol. 41 (3), 523–540.

Bornemann, A., Norris, R.D., Lyman, J.A., D'haenens, S., Groeneveld, J., Röhl, U., Speijer, R.P., 2014. Persistent environmental change after the Paleocene–Eocene Thermal Maximum in the eastern North Atlantic. Earth Planet. Sci. Lett. 394, 70–81.

Charles, A.J., Condon, D.J., Harding, I.C., Pälike, H., Marshall, J.E., Cui, Y., Croudace, I.W., 2011. Constraints on the numerical age of the Paleocene-Eocene boundary. Geochem. Geophys. Geosyst. 12 (6).

Cramer, B.S., Toggweiler, J.R., Wright, J.D., Katz, M.E., Miller, K.G., 2009. Ocean overturning since the Late Cretaceous: inferences from a new benthic foraminiferal isotope compilation. Paleoceanography 24 (4).

Cramwinckel, M.J., Huber, M., Kocken, I.J., Agnini, C., Bijl, P.K., Bohaty, S.M., Peterse, F., 2018. Synchronous tropical and polar temperature evolution in the Eocene. Nature 559 (7714), 382–386.

Dickens, G.R., O'Neil, J.R., Rea, D.K., Owen, R.M., 1995. Dissociation of oceanic methane hydrate as a cause of the carbon isotope excursion at the end of the Paleocene. Paleoceanogr. Paleoclimatol. 10 (6), 965–971.

Dunkley Jones, T., Lunt, D.J., Schmidt, D.N., Ridgwell, A., Sluijs, A., Valdes, P.J., Maslin, M., 2013. Climate model and proxy data constraints on ocean warming across the Paleocene–Eocene Thermal Maximum. Earth-Sci. Rev. 125, 123–145.

Fleming, L.E., Tierney, J.E., 2016. An automated method for the determination of the TEX86 and U37K′ paleotemperature indices. Org. Geochem. 92, 84–91.

Frieling, J., Iakovleva, A.I., Reichart, G.J., Aleksandrova, G.N., Gnibidenko, Z.N., Schouten, S., Sluijs, A., 2014. Paleocene–Eocene warming and biotic response in the epicontinental West Siberian Sea. Geology 42 (9), 767–770.

Frieling, J., Svensen, H.H., Planke, S., Cramwinckel, M.J., Selnes, H., Sluijs, A., 2016. Thermogenic methane release as a cause for the long duration of the PETM. Proc. Natl. Acad. Sci. 113 (43), 12059–12064.

Frieling, J., Gebhardt, H., Huber, M., Adekeye, O.A., Akande, S.O., Reichart, G.J., Sluijs, A., 2017. Extreme warmth and heat-stressed plankton in the tropics during the Paleocene-Eocene Thermal Maximum. Sci. Adv. 3 (3), e1600891.

Frieling, J., Peterse, F., Lunt, D.J., Bohaty, S.M., Sinninghe Damsté, J.S., Reichart, G.J., Sluijs, A., 2019. Widespread warming before and elevated barium burial during the Paleocene-Eocene Thermal Maximum: evidence for methane hydrate release? Paleoceanogr. Paleoclimatol. 34 (4), 546–566.

Gutjahr, M., Ridgwell, A., Sexton, P.F., Anagnostou, E., Pearson, P.N., Pälike, H., Foster, G.L., 2017. Very large release of mostly volcanic carbon during the Palaeocene–Eocene Thermal Maximum. Nature 548 (7669), 573–577.

Heilmann-Clausen, C., Nielsen, O.B., Gersner, F., 1985. Lithostratigraphy and depositional environments in the Upper Paleocene and Eocene of Denmark. Bull. Geol. Soc. Den. 33, 287–323.

Hollis, C.J., Dunkley Jones, T., Wade, B.S., 2019. The DeepMIP contribution to PMIP4: methodologies for selection, compilation and analysis of latest Paleocene and early Eocene climate proxy data, incorporating version 0.1 of the DeepMIP database. Geosci. Model Dev. Discuss.

Hopmans, E.C., Weijers, J.W., Schefuß, E., Herfort, L., Damsté, J.S.S., Schouten, S., 2004. A novel proxy for terrestrial organic matter in sediments based on branched and isoprenoid tetraether lipids. Earth Planet. Sci. Lett. 224 (1–2), 107–116.

Hopmans, E.C., Schouten, S., Damsté, J.S.S., 2016. The effect of improved chromatography on GDGT-based palaeoproxies. Org. Geochem. 93, 1–6.

Inglis, G.N., Farnsworth, A., Collinson, M.E., Carmichael, M.J., Naafs, B.D.A., Lunt, D.J., Pancost, R.D., 2019. Terrestrial environmental change across the onset of the PETM and the associated impact on biomarker proxies: a cautionary tale. Glob. Planet. Change 181, 102991.

Inglis, G.N., Bragg, F., Burls, N., Evans, D., Foster, G.L., Huber, M., Lunt, D.J., Siler, N., Steinig, S., Wilkinson, R., Anagnostou, E., Cramwinckel, M., Hollis, C.J., Pancost, R.D., Tierney, J., 2020. Global mean surface temperature and climate sensitivity of the EECO, PETM and latest Paleocene. Clim. Paste. https://doi.org/10.5194/cp-2019-167 (in press).

John, C.M., Bohaty, S.M., Zachos, J.C., Sluijs, A., Gibbs, S., Brinkhuis, H., Bralower, T.J., 2008. North American continental margin records of the Paleocene-Eocene thermal maximum: implications for global carbon and hydrological cycling. Paleoceanography 23 (2).

Jolley, D.W., Widdowson, M., 2005. Did Paleogene North Atlantic rift-related eruptions drive early Eocene climate cooling? Lithos 79, 355–366.

Jones, M.T., Jerram, D.A., Svensen, H.H., Grove, C., 2016. The effects of large igneous provinces on the global carbon and sulphur cycles. Palaeogeogr. Palaeoclimatol. Palaeoecol. 441, 4–21.

Jones, M.T., Percival, L.M., Stokke, E.W., Frieling, J., Mather, T.A., Riber, L., Svensen, H.H., 2019. Mercury anomalies across the Palaeocene–Eocene thermal maximum. Clim. Past 15 (1).

Kender, S., Stephenson, M.H., Riding, J.B., Leng, M.J., Knox, R.W.B., Peck, V.L., Jamieson, R., 2012. Marine and terrestrial environmental changes in NW Europe preceding carbon release at the Paleocene–Eocene transition. Earth Planet. Sci. Lett. 353, 108–120.

Kim, J.H., Van der Meer, J., Schouten, S., Helmke, P., Willmott, V., Sangiorgi, F., Damsté, J.S.S., 2010. New indices and calibrations derived from the distribution of crenarchaeal isoprenoid tetraether lipids: implications for past sea surface temperature reconstructions. Geochim. Cosmochim. Acta 74 (16), 4639–4654.

King, C., 2016. A Revised Correlation of Tertiary Rocks in the British Isles and Adjacent Areas of NW Europe (Gale, A.S. & Barry, T.L., editors). Special Reports, vol. 27. The Geological Society, London.

Knox, R.W.O'B., Bosch, J.H.A., Rasmussen, E.S., Heilmann-Clausen, C., Hiss, M., De Lugt, I.R., Kasinski, J., King, C., Köthe, A., Slodkowska, B., Standke, G., Vandenberghe, N., 2010. Cenozoic. In: Dornenbaal, H., Stevenson, A. (Eds.), Petroleum Geological Atlas of the Southern Permian Basin Area. EAGE Publications b.v, Houten, pp. 211–223.

Larsen, R.B., Tegner, C., 2006. Pressure conditions for the solidification of the Skaergaard intrusion: eruption of East Greenland flood basalts in less than 300,000 years. Lithos 92 (1–2), 181–197.

Larsen, L.M., Fitton, J.G., Pedersen, A.K., 2003. Paleogene volcanic ash layers in the Danish Basin: compositions and source areas in the North Atlantic Igneous Province. Lithos 71 (1), 47–80.

Littler, K., Röhl, U., Westerhold, T., Zachos, J.C., 2014. A high-resolution benthic stable-isotope record for the South Atlantic: implications for orbital-scale changes in Late Paleocene–Early Eocene climate and carbon cycling. Earth Planet. Sci. Lett. 401, 18–30.

Ma, Z., Gray, E., Thomas, E., Murphy, B., Zachos, J., Paytan, A., 2014. Carbon sequestration during the Palaeocene–Eocene Thermal Maximum by an efficient biological pump. Nat. Geosci. 7 (5), 382–388.

McInerney, F.A., Wing, S.L., 2011. The Paleocene-Eocene Thermal Maximum: a perturbation of carbon cycle, climate, and biosphere with implications for the future. Annu. Rev. Earth Planet. Sci. 39, 489–516.

Ogg, J., 2012. Geomagnetic polarity time scale. In: Gradstein, F., Ogg, J., Schmitz, M., Ogg, G. (Eds.), The Geologic Time Scale 2012. Elsevier, pp. 85–113.

Peters, K.E., Peters, K.E., Walters, C.C., Moldowan, J.M., 2005. The Biomarker Guide (vol. 1). Cambridge University Press.

Peterse, F., Kim, J.H., Schouten, S., Kristensen, D.K., Koç, N., Damsté, J.S.S., 2009. Constraints on the application of the MBT/CBT palaeothermometer at high latitude environments (Svalbard, Norway). Org. Geochem. 40 (6), 692–699.

Robock, A., 2000. Volcanic eruptions and climate. Rev. Geophys. 38, 191–219.

Schaller, M.F., Fung, M.K., Wright, J.D., Katz, M.E., Kent, D.V., 2016. Impact ejecta at the Paleocene-Eocene boundary. Science 354 (6309), 225–229.

Schmidt, A., Skeffington, R.A., Thordarson, T., Self, S., Forster, P.M., Rap, A., Ridgwell, A., Fowler, D., Wilson, M., Mann, G.W., Wignall, Paul B., Carslaw, K.S., 2016. Selective environmental stress from sulphur emitted by continental flood basalt eruptions. Nat. Geosci. 9, 77–82.

Schmitz, B., Peucker-Ehrenbrink, B., Heilmann-Clausen, C., Åberg, G., Asaro, F., Lee, C.T.A., 2004. Basaltic explosive volcanism, but no comet impact, at the Paleocene–Eocene boundary: high-resolution chemical and isotopic records from Egypt, Spain and Denmark. Earth Planet. Sci. Lett. 225 (1–2), 1–17.

Schoon, P.L., Heilmann-Clausen, C., Schultz, B.P., Damsté, J.S.S., Schouten, S., 2015. Warming and environmental changes in the eastern North Sea Basin during the Palaeocene–Eocene Thermal Maximum as revealed by biomarker lipids. Org. Geochem. 78, 79–88.

Schouten, S., Hopmans, E.C., Schefuß, E., Damste, J.S.S., 2002. Distributional variations in marine crenarchaeotal membrane lipids: a new tool for reconstructing ancient sea water temperatures? Earth Planet. Sci. Lett. 204 (1–2), 265–274.

Sluijs, A., Schouten, S., Pagani, M., Woltering, M., Brinkhuis, H., Damsté, J.S.S., Matthiessen, J., 2006. Subtropical Arctic Ocean temperatures during the Palaeocene/Eocene thermal maximum. Nature 441 (7093), 610.

Sluijs, A., Bijl, P.K., Schouten, S., Röhl, U., Reichart, G.J., Brinkhuis, H., 2011. Southern ocean warming, sea level and hydrological change during the Paleocene-Eocene thermal maximum. Clim. Past 7 (1), 47–61.

Storey, M., Duncan, R.A., Swisher, C.C., 2007a. Paleocene-Eocene thermal maximum and the opening of the northeast Atlantic. Science 316 (5824), 587–589.

Storey, M., Duncan, R.A., Tegner, C., 2007b. Timing and duration of volcanism in the North Atlantic Igneous Province: implications for geodynamics and links to the Iceland hotspot. Chem. Geol. 241 (3), 264–281.

Svensen, H., Planke, S., Malthe-Sørenssen, A., Jamtveit, B., Myklebust, R., Eidem, T.R., Rey, S.S., 2004. Release of methane from a volcanic basin as a mechanism for initial Eocene global warming. Nature 429 (6991), 542.

Thordarson, T., Self, S., 2003. Atmospheric and environmental effects of the 1783–1784 Laki eruption: a review and reassessment. J. Geophys. Res., Atmos. 108 (D1), AAC-7.

Tierney, J.E., Tingley, M.P., 2014. A Bayesian, spatially-varying calibration model for the TEX86 proxy. Geochim. Cosmochim. Acta 127, 83–106.

van der Meulen, B., Gingerich, P.D., Lourens, L.J., Meijer, N., van Broekhuizen, S., van Ginneken, S., Abels, H.A., 2020. Carbon isotope and mammal recovery from extreme greenhouse warming at the Paleocene–Eocene boundary in astronomically-calibrated fluvial strata, Bighorn Basin, Wyoming, USA. Earth Planet. Sci. Lett. 534, 116044.

Weijers, J.W., Schouten, S., Spaargaren, O.C., Sinninghe Damsté, J.S., 2006. Occurrence and distribution of Tetraether membrane lipids in soils: implications for the use of the TEX86 proxy and the BIT index. Org. Geochem. 37 (10), 1680–1693.

Westerhold, T., Röhl, U., McCarren, H.K., Zachos, J.C., 2009. Latest on the absolute age of the Paleocene–Eocene Thermal Maximum (PETM): new insights from exact stratigraphic position of key ash layers +19 and −17. Earth Planet. Sci. Lett. 287 (3–4), 412–419.

Westerhold, T., Röhl, U., Wilkens, R.H., Gingerich, P.D., Clyde, W.C., Wing, S.L., Bowen, G.J., Kraus, M.J., 2018. Synchronizing early Eocene deep-sea and continental records – cyclostratigraphic age models for the Bighorn Basin Coring Project drill cores. Clim. Past 14, 303–319.

Wieczorek, R., Fantle, M.S., Kump, L.R., Ravizza, G., 2013. Geochemical evidence for volcanic activity prior to and enhanced terrestrial weathering during the Paleocene Eocene Thermal Maximum. Geochim. Cosmochim. Acta 119, 391–410.

Zachos, J.C., Schouten, S., Bohaty, S., Quattlebaum, T., Sluijs, A., Brinkhuis, H., Bralower, T.J., 2006. Extreme warming of mid-latitude coastal ocean during the Paleocene-Eocene Thermal Maximum: inferences from TEX86 and isotope data. Geology 34 (9), 737–740.

Zachos, J.C., McCarren, H., Murphy, B., Röhl, U., Westerhold, T., 2010. Tempo and scale of late Paleocene and early Eocene carbon isotope cycles: implications for the origin of hyperthermals. Earth Planet. Sci. Lett. 299 (1–2), 242–249.

Zeebe, R.E., Lourens, L.J., 2019. Solar System chaos and the Paleocene–Eocene boundary age constrained by geology and astronomy. Science 365 (6456), 926–929.

Zhang, Y.G., Zhang, C.L., Liu, X.L., Li, L., Hinrichs, K.U., Noakes, J.E., 2011. Methane index: a tetraether archaeal lipid biomarker indicator for detecting the instability of marine gas hydrates. Earth Planet. Sci. Lett. 307 (3–4), 525–534.

Zhang, Y.G., Pagani, M., Wang, Z., 2016. Ring index: a new strategy to evaluate the integrity of TEX86 paleothermometry. Paleoceanography 31 (2), 220–232.